JOURNAL OF SPACECRAFT AND ROCKETS
Vol. 38, No. 3, May–June 2001

Near- and Far-Field Characterization of Stationary Plasma Thruster Plumes

Alec D. Gallimore*
University of Michigan, Ann Arbor, Michigan 48109-2140

A comprehensive investigation of Hall thruster plume plasma ion energy distribution functions and ion charge state has been made on both flight- and laboratory-model engines. An energy analyzer, mass spectrometer, and $E \times B$ probe were used to characterize Hall thruster plume ions. The results of this investigation show that the distribution function of the ion beam exhibits both Maxwellian and Druyvesteyn traits and that the Hall thruster plume contains a nontrivial amount of energetic, multiply charged particles that must be accounted for in modeling the erosion rate of solar array cover glass and interconnect material. Detection of these multiply charged ions by energy analyzers has been hampered in the past by charge exchange and elastic collisions. The high-energy tail seen in numerous energy analyzer data is thought to result from charge exchange and elastic collisions between singly and multiply charged ions and neutrals. The role of facility pressure was also investigated and was found to have an influence mainly on the width of the ion energy distribution function. This pressure broadening is caused by elastic collisions between beam ions and background chamber gas particles.

Nomenclature

$\boldsymbol{B}$	=	magnetic field vector, T
E	=	electric field, V/m
$\boldsymbol{E}$	=	electric field vector, V/m
E_b	=	ion beam energy, eV
E_i	=	ion energy, eV
f	=	ion distribution function
$f(E_i)$	=	ion energy distribution function
$f(\boldsymbol{v})$	=	ion velocity distribution function
I_i	=	$\boldsymbol{E} \times \boldsymbol{B}$ probe collector current, A
n_i	=	ion number density, m^{-3}
q	=	elementary charge, C
q_I	=	charge state of ion
$\boldsymbol{r}$	=	position vector, m
t	=	time, s
u_i	=	ion speed, m/s
V_i	=	beam ion acceleration potential, V
$\boldsymbol{v}$	=	ion velocity vector, m/s

Introduction

BECAUSE of their efficient use of propellant in producing thrust, advanced spacecraft propulsion systems such as the Hall thruster can significantly enhance a variety of commercial and scientific space missions. Such mission enhancement is done by increasing mission life or payload mass for a given amount of fuel or, with fixed ΔV or payload requirements, reducing initial spacecraft mass. These features either enable space missions to occur by providing sufficient performance that is otherwise unattainable, or enhance space missions by reducing trip time and/or launch costs through decreased spacecraft mass.

Studies have shown that ideally an engine that would be used as the primary source of propulsion for orbit transfer missions or for north–south station keeping (NSSK) should produce an exhaust velocity between 10 and 20 km/s (Ref. 1), that is, a specific impulse between 1000 and 2000 s. Cryogenic chemical rocket motors are capable of producing specific impulses of 480 s or less,[2] and space-storable chemical engines that are currently used on spacecraft have even lower specific impulses[2] (approximately 330 s). Hall thrusters, with specific impulses between 1500 and 2500 s and efficiencies above 50%, are well suited for station-keeping, orbit-raising, and orbit-transfer (including deorbiting) applications in Earth orbit. As such, there is great interest in integrating these engines with commercial and military spacecraft.

Because the energetic ions that emerge from the engine could damage sensitive spacecraft systems such as solar arrays and optics, it is essential that the plume of these devices are suitably characterized to allow for the successful incorporation of Hall thrusters on spacecraft. Moreover, fundamental information on plasma transport properties, ion energy distributions, and ionic charge state are needed by modelers and thruster designers alike to understand better how Hall thrusters work and to improve these engines.

This paper reviews work done at the University of Michigan to characterize the ion energy distribution and ionic charge state in the plumes of two Hall thrusters, the flight-model SPT-100 and the laboratory-model P5, using a mass spectrometer, an energy analyzer, and an $\boldsymbol{E} \times \boldsymbol{B}$ probe. Work done with the SPT-100 thruster is reviewed, whereas the section that subsequently follows concentrates on results obtained with the P5 engine. Before discussing the results of these thruster plume investigations, it is worthwhile to review Hall thruster physics because it clearly relates to plume dynamics.

Hall Thruster

The Hall thruster is an electrostatic engine that was developed in the 1960s to alleviate the thrust density limitation of ion thrusters that results from space-charge effects within the acceleration volume between the grids. Hall thrusters were also attractive from the standpoint that, because grids are not required to accelerate ions, they do not suffer from the large grid erosion rates of ion thrusters. Interest in the Hall thruster waned in the early 1970s, however, because of budgetary cuts and because American researchers were never able to demonstrate that these engines could operate at thrust efficiencies near those achieved with ion thrusters.[3–5] As such, Hall thruster research essentially disappeared in the United States between 1972 and 1985. From 1985 to 1990, Ford Aerospace [now Space Systems/Loral (SS/L)], in conjunction with the NASA Lewis Research Center [now the John H. Glenn Research Center at Lewis Field (GRC)], funded a small research effort to determine if Hall thrusters could be used for NSSK.[6] This program proved to be unsuccessful and was abandoned.

Throughout this period, however, Hall thruster research flourished in the Soviet Union, ironically partly because their engineers were never able to develop adequate grids for ion thrusters. Hall thrusters were first tested in space in 1971 with immediate success.[7,8] Since then, over 100 Hall thrusters have been used on Soviet and later Russian spacecraft, mostly as plasma contactors and for east–west

Received 14 July 2000; revision received 11 December 2000; accepted for publication 19 December 2000.

*Associate Professor and Director, Plasmadynamics and Electric Propulsion Laboratory, Department of Aerospace Engineering, 1320 Beal Avenue. Associate Fellow AIAA.

station keeping. However, in 1994, the first satellite to use Hall thrusters for NSSK was launched by Russia. Because of this and numerous experiments that show that Russian Hall thrusters are capable of generating specific impulses above 1500 s at thrust efficiencies of 50% or more,[9] there has been a great deal of interest in using these engines on American spacecraft for NSSK and for orbit repositioning. Clearly this device would not only serve as an excellent thruster for orbit station-keeping and repositioning roles, but potentially could be scaled in power to propel orbit transfer vehicles and planetary probes.

Closed-Drift Hall Thruster

There are two types of Hall thrusters that have been studied at great lengths: the end-Hall thruster and the closed-drift Hall thruster (CDT). Both engines, in principle, are capable of producing specific impulses in excess of 1500 s with xenon at a thrust efficiency of 50% or greater. However, it is the CDT, which has been developed and used in the former Soviet Union over the past 40 years, that is of the most interest to the Western space technology community.

The CDT is a coaxial device in which a magnetic field that is produced by an electromagnet is channeled between an inner ferromagnetic core (pole piece) and outer ferromagnetic ring (Fig. 1). This configuration results in an essentially radial magnetic field with a peak strength of a few hundred gauss. This field strength is such that only the electrons are magnetized. In addition, an axial electric field is provided by applying a voltage between the anode and the downstream cathode. As the electrons stream upstream from the cathode to the anode, the $\boldsymbol{E} \times \boldsymbol{B}$ action on the electrons causes them to drift in the azimuthal direction, forming a Hall current. Through collisions, these electrons ionize propellant molecules that are injected through the anode and that are subsequently accelerated by the axial electric field. The mixture of electrons and ions in the acceleration zone means that the plasma is electrically neutral, and as such, is not space-charge limited in ion current density. Because the magnetic field suppresses the axial mobility of the electrons while exerting essentially no effect on ion motion, the plasma can support an axial electric field with a potential difference close to the applied voltage between the electrodes. Thus, the bulk of the ions are accelerated to kinetic energies to within 80% of the applied discharge voltage.[9] This combination of processes accounts for the CDT's high thrust efficiency.

To first order, magnetic field lines are parallel with equipotential lines. Thus, the former influences the latter. Because ions are accelerated by the electric field, the magnetic field topology clearly has a strong influence on ion plume dynamics and, hence, on spacecraft interaction issues. This process holds true, as we will see later, regardless of the ion charge state.

Russian CDTs come in two variants: the stationary plasma thruster (SPT) (also known as the magnet layer thruster) and the anode layer thruster (TAL). The main difference between these two devices is that the SPT uses a dielectric coating that usually contains boron nitride to insulate electrically its acceleration channel walls, whereas the TAL uses a channel made out of an electrical conductor such as graphite. The specific impulse and thrust efficiency characteristics of both engines are similar.[3] Although they vary in size and input power, CDTs that are currently being considered for NSSK typically operate at discharge voltages of 300–350 V and thruster currents between 4.5 and 15 A, with xenon mass flow rates of 5–18 mg/s.

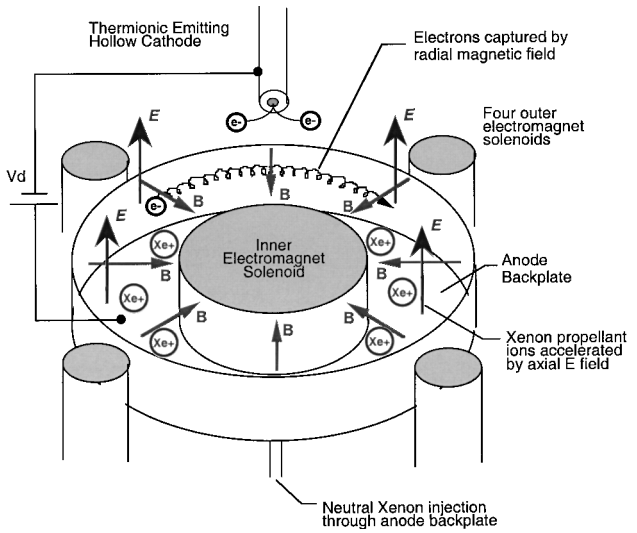

Fig. 1 Schematic of a CDT.

Motivation

The configuration of three-axis-stabilized communication satellites is such that part of the plume of a Hall thruster used for NSSK will impact the solar arrays of the spacecraft, which can have a negative influence on spacecraft operations and life. Sputtering-induced erosion of antireflective solar cell cover glass coatings can degrade solar array performance by a few percent.[10] Erosion of solar cell interconnects can increase the resistivity of the array circuit and reduce array performance. Whereas researchers have relied on sample exposure tests and computational modeling to predict the impact that plume impingement on spacecraft solar array material will have on spacecraft operations, these efforts have been hampered by facility effects and the need to make simplifying assumptions about the plume.[10,11] These assumptions could lead to large uncertainties at best and a serious underprediction of solar array erosion at worst.

Researches in the past have shown that Hall thruster plumes consist of multiply charged ions.[12] The production of multiply charged ions in the thruster discharge chamber not only represents a loss mechanism in terms of thrust, efficiency, and mass utilization,[13] but also causes more damage to the discharge chamber walls and adjacent spacecraft surfaces due to the higher energy of the multiply charged ions. Therefore, it is essential that the distribution of the energy and charge state of the plume ions is measured and incorporated into the appropriate models to make a more accurate assessment of solar array erosion.

The microscopic or kinetic properties of a plasma can be described by one basic term, the distribution function $f(\boldsymbol{v}, \boldsymbol{r}, t)$. Macroscopic parameters such as density, temperature, and transport properties can all be derived from $f(\boldsymbol{v}, \boldsymbol{r}, t)$ by forming its moments, that is, integrals over velocity space. As such, it is obvious that, for a multi-charge state plasma such as a Hall thruster plume, the distribution function of each ion species is needed to characterize fully the plasma properties. Therefore, it is of great interest to obtain $f(\boldsymbol{v}, \boldsymbol{r}, t)$ of each ion charge state in the plasma. For a quasi-steady plasma such as the Hall thruster plume, one tries to find $f(\boldsymbol{v})$ or $f(E_i)$ in the plasma to derive the macroscopic parameters.

In spite of the importance of $f(E_i)$ to kinetic theories, there are only a few means for direct measurement of $f(E_i)$. The most commonly used device for measuring the ion energy distribution function is the retarding potential analyzer (RPA).[14] However, the raw RPA data must be differentiated numerically to obtain the energy distribution, and thus, the noise of the raw data is magnified when the resulting distribution curves are calculated. Furthermore, the RPA technique cannot distinguish different ion species in the thruster plume. Thus, our investigation has concentrated on using species-differentiating techniques in characterizing the Hall thruster plume. This paper will first review SPT-100 Hall thruster far-field plume data taken with a molecular beam mass spectrometer (MBMS) and an $\boldsymbol{E} \times \boldsymbol{B}$ probe and then review P5 laboratory-model Hall thruster near- and far-field plume data collected with the MBMS at an order of magnitude lower tank pressure.

Far-Field Experiments with the SPT-100

Apparatus for Far-Field SPT-100 Tests

The thruster used for all experiments described in this section was a flight-model SPT-100 stationary plasma thruster manufactured by the Fakel Design Bureau of Russia. The thruster was operating at its nominal conditions of 300 V at 4.5 A throughout the investigation. A total xenon flow rate of 5.5 mg/s, with 7% of this going through the hollow cathode distribution system, was used for all tests. The thruster electrical discharge and magnetic field circuitry

was controlled by a breadboard power processing unit (PPU) manufactured by SS/L. The PPU was powered by a 55-V–55-A commercial (Sorenson) power supply used to simulate the bus of a communication satellite. Thruster current and voltage were measured to an accuracy of within 1% of the true value with commercial multimeters.

High-purity (99.999% pure) xenon propellant was supplied to the Hall thruster from compressed gas bottles through stainless-steel feed lines. Propellant flow was controlled and monitored with MKS 1159B mass flow controllers specifically calibrated for xenon. The flow controllers were periodically calibrated with an apparatus that measures gas pressure and temperature as a function of time in an evacuated chamber of known volume. The system is capable of providing up to 12 mg/s of xenon with an accuracy to within 0.1 mg/s of the true value.

Experiments were conducted in a 9-m-long × 6-m-diam stainless-steel vacuum chamber known as the Large Vacuum Test Facility (LVTF) (Fig. 2). At the time, the LVTF was pumped by six 81-cm-diam oil diffusion pumps backed by two 1000 l/s blowers and four 200 l/s mechanical pumps for a xenon pumping speed of approximately 20,000 l/s. During the thruster operation, the background pressure was approximately 7×10^{-3} Pa (5×10^{-5} torr) (xenon) as indicated by MKS model 919 hot-cathode ionization gauges that were corrected for xenon. These gauges were located on two vacuum ports on either side of the chamber and inside the chamber near the center of the tank. The chamber base pressure was roughly 3×10^{-3} Pa (2×10^{-5} torr) (air) for these tests.

Our investigation concentrated on using species-differentiating techniques in characterizing the Hall thruster plume. The first of these is the MBMS. The MBMS (Fig. 3) is a time-of-flight mass spectrometer with a 45-deg parallel plate energy analyzer. It is essentially two instruments in one that when used together can give direct measurements of both ion energy and species composition.

The mass spectrometer is mounted to one end of the LVTF. A 20-cm-diam stainless-steel gate valve was placed between the energy analyzer chamber and the main vacuum tank enabling rapid venting and repumping of the MBMS for configuration adjustments without impacting the LVTF vacuum.

Ions pass into the MBMS through a sampling orifice fashioned from 304 stainless-steel plates drilled and countersunk from the downstream face. This created a very thin-edged orifice to minimize skimmer wall effects. King[15] showed that less than 5% of the ion beam entering the MBMS will experience charge exchange collisions within the neutral ram cloud of atoms immediately upstream of the MBMS sampling skimmer. To minimize the probability of collisions between beam ions and background gas particles, the two subchambers of the MBMS were evacuated by a Varian HS-10 25-cm-diam oil diffusion pump and a Varian M6 15-cm-diam oil diffusion pump. Both diffusion pumps used Dow–Corning 705 pump oil and were fitted with conductively cooled halo baffles at the inlet to minimize oil backstreaming into the MBMS volume. The two diffusion pumps were backed by a 40 l/s Kinney KDH-80 rotary mechanical pump. The MBMS internal pressure was monitored by one thermocouple pressure sensor and two hot-cathode ionization pressure gauges. A pressure of 4×10^{-5} Pa (3×10^{-7} torr) was maintained within the MBMS volume for all tests. Graphoil was placed around the chamber wall adjacent to the MBMS to minimize sputtering of tank wall material.

To measure the energy distribution, the ion plume enters the 45-deg energy analyzer, which allows ions of a specific energy-to-charge ratio E/q to pass through and reach the detector. This ratio is selected by setting the voltage between the plates of the analyzer. By sweeping the voltage, an entire ion energy distribution function can be determined without the need for any numerical differentiation as with an RPA. The energy resolution of the instrument is better than an electron volt.

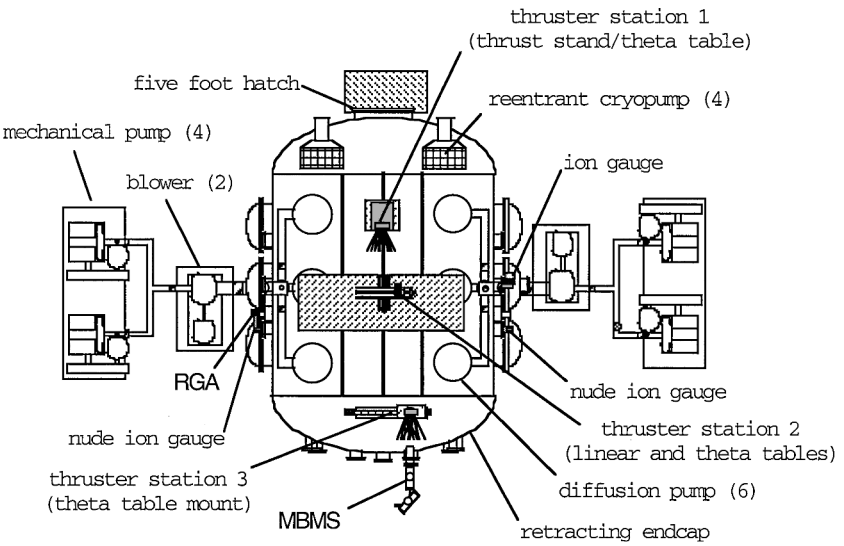

Fig. 2 Schematic of the LVTF.

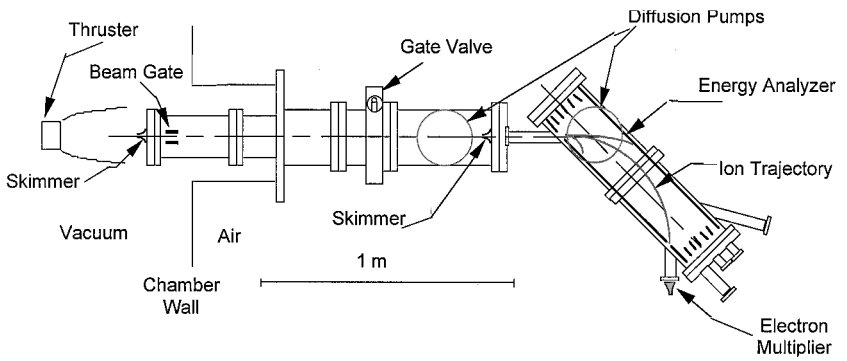

Fig. 3 Schematic of the MBMS in configuration used for far-field SPT-100 plume characterization.

For species composition, the time-of-flight mass spectrometer mode of the MBMS is used wherein an electrostatic beam gate is placed downstream of the sampling orifice. When the gate is pulsed open and the time is recorded that it takes for the ions to reach the detector at the end of the energy analyzer for a given pass voltage, that is, E/q, the individual species of the plasma can be detected. The mass resolution of the instrument is approximately an atomic mass unit (AMU). These two capabilities enable the MBMS to measure the energy distribution of multiply charged ions. Further details of the MBMS may be found in Ref 15.

The second species-differentiating diagnostic used was the $\boldsymbol{E} \times \boldsymbol{B}$ probe, also known as a Wien filter. An $\boldsymbol{E} \times \boldsymbol{B}$ probe utilizes uniform crossed electric and magnetic fields that are perpendicular to each other and the particle velocity vector. Thus, the two fields and the particle velocity vector form orthogonal axes. The $\boldsymbol{E} \times \boldsymbol{B}$ probe is a simple diagnostic technique that can separate different ion species according to their velocities provided that they are all accelerated by the same electric field. Because the MBMS 45-deg energy analyzer is sensitive only to ions of differing E/q, the velocity-sensitive $\boldsymbol{E} \times \boldsymbol{B}$ probe provides additional insight on plume dynamics.

Use of the $\boldsymbol{E} \times \boldsymbol{B}$ probe in electric propulsion research had been limited to the investigations of ion thrusters.[16–22] In those studies, the $\boldsymbol{E} \times \boldsymbol{B}$ probe was utilized to measure the ratio of doubly to singly charged ions to provide thrust correction factors and the optimal operating condition for minimum production of multiply charged ions. Ion thruster plume ions are essentially monoenergetic particles. As such, the ion ratio was calculated directly from the heights of the narrow probe trace peaks of each species. The ions in the Hall thruster plume, on the other hand, are produced at different positions in the discharge chamber and, thus, experience different acceleration voltages. Therefore, the resulting probe trace peaks will have some structure that must be accounted for in the analysis. Because the ion velocities are related to their energies, the measured probe traces were curve fitted with a distribution function model based on the kinetic theory of gases to obtain ion energy distribution functions of each ion species at various locations in the thruster plume. The study reported here is the first attempt to use an $\boldsymbol{E} \times \boldsymbol{B}$ probe to obtain the ion energy distributions in the Hall thruster plume. A detailed description of the probe may be found in Ref. 23. The total uncertainty in the ion energy distribution measurements is estimated to be $\pm 2\%$ for the ion current and $\pm 4\%$ for the ion energy.

For both the MBMS and $\boldsymbol{E} \times \boldsymbol{B}$ probe tests, the probe remained fixed while the thruster was moved about with a custom-made probe positioning system developed by New England Affiliated Technologies (NEAT). The probe positioning table has two degrees of freedom as well as angular freedom in the horizontal plane, that is, radial, axial, and θ. The table contains two rotary platforms on a 1.8-m-long linear stage in the radial direction that is mounted on a 0.9-m-long axial stage with an absolute linear position accuracy of 0.15 mm and an angular position accuracy of 0.1 deg. The actual position accuracy for these tests, as determined by a laser alignment system was 0.5 deg (Ref. 15). For MBMS tests, the thruster was placed on a NEAT rotary platform that remained fixed with respect to the tank wall at thruster station 3 (see Fig. 2). This allowed the thruster to be rotated 360 deg about its centerline axis in yaw. The thruster was placed on the rotary and linear tables at thruster station 2 for the $\boldsymbol{E} \times \boldsymbol{B}$ probe tests.

SPT-100 Results

One of the most puzzling aspects of ion energy measurements taken with RPAs in the plume of Hall thrusters is the so-called high-energy tail, that is, the significant fraction of probe ion current present at energies above the discharge voltage of the thruster. For example, it is not uncommon to detect ions at kinetic energies above 400 V while the thruster voltage is only 300 V (Refs. 15, 24, and 25). Although a number of theories have been postulated to explain the existence of the tail, including plasma instability-driven turbulence within the thruster discharge as well as recombinative or charge-changing collisions within the exhaust plume, it was only fairly recently that a solution to this problem was presented. In fact, it will be shown subsequently that the structure of the ion energy distribution function, particularly the high-energy tail, provides a wealth of information about plasma and collisional processes both in the plume and within the thruster.

King[15] performed a comprehensive characterization of the ion energy distribution function of the SPT-100 using both RPAs and the MBMS. It was concluded that the tail is a result of both charge exchange and elastic collisions between neutrals, singly, and multiply charged plume ions. Specifically, the Hall thruster accelerates singly, doubly, and triply charged xenon ions to high energies. These particles experience charge exchange and elastic collisions in the plume of the thruster both among themselves and with ambient chamber and thruster neutrals. Other collisional processes such as ionization and recombination were quickly discounted because their collision probabilities in the plume were negligible in comparison to those of charge exchange and elastic collisions.[26]

To illustrate the role of charge exchange collision in affecting the ion energy distribution, let us consider the example of a doubly charged ion that is accelerated by a potential V_i (and, hence, to an energy of $2qV_i$) that undergoes a charge exchange collision with a neutral atom with negligible velocity. There are two possible outcomes to this event. First, two electrons could be transferred from the neutral atom to the ion, neutralizing the latter. This process would result in a doubly charged ion with random near-zero velocity, which would likely not reach the detector, and a neutral with a directed energy of $2V_i$ that cannot be detected by the analyzer because it has no net charge. Thus, the first outcome results in products that cannot be detected. The second outcome, however, can be observed if instead one electron is transferred to the doubly charged ion. The resulting singly charged ion would have twice the energy of a normally produced singly charged ion and, thus, would appear in the E/q domain of the MBMS or RPA at twice the most probable voltage found in the main distribution.

This scenario is quite plausible given that the relevant mean free paths at a chamber pressure of 7×10^{-3} Pa (Table 1) are on the order of 1 m considering only background gas particles and that the near-field neutral pressure of the SPT-100 is an order of magnitude higher still. At this pressure, the background neutral number density in the chamber is approximately 1×10^{18} m^{-3}, whereas the SPT-100 exit plane neutral density is approximately 1×10^{19} m^{-3}. All collision cross section data used to generate Table 1 are from Ref. 26. The detectable products for ion–neutral charge exchange collisions are given in Table 2 for collisions between single, double, triple, and quadruple ions accelerated by a potential V_i with zero velocity background neutral xenon.[26]

To illustrate ion–ion charge exchange phenomena, we consider a charge exchange collision between a doubly and a singly charged ion, both created deep within a Hall thruster. The doubly charged ion

Table 1 Mean free paths (MFP) for 6.7×10^{-3} Pa (5.0×10^{-5} torr) tank pressure

Collision	Chamber MFP, m
$Xe^+ + Xe$ charge exchange	1.2
$Xe^{2+} + Xe$ charge exchange	0.9
Electron–electron elastic	5.1
Electron–ion elastic	4.9
Ion–ion elastic	1.2
Ion–electron elastic	6.4
Ion–neutral elastic	10.5
Electron–neutral elastic	3.2
Neutral–neutral elastic	1.4

Table 2 Ion–neutral charge exchange collision products[26]

Reaction	Detectable product	Electrons transferred
$Xe^+ + Xe$	None	1
$Xe^{2+} + Xe$	Xe^+ at $E_i/q_i = 2V_i$	1
$Xe^{3+} + Xe$	Xe^{2+} at $E_i/q_i = 3/2V_i$	1
$Xe^{3+} + Xe$	Xe^+ at $E_i/q_i = 3V_i$	2
$Xe^{4+} + Xe$	Xe^{3+} at $E_i/q_i = 4/3V_i$	1
$Xe^{4+} + Xe$	Xe^{2+} at $E_i/q_i = 2V_i$	2
$Xe^{4+} + Xe$	Xe^+ at $E_i/q_i = 4V_i$	3

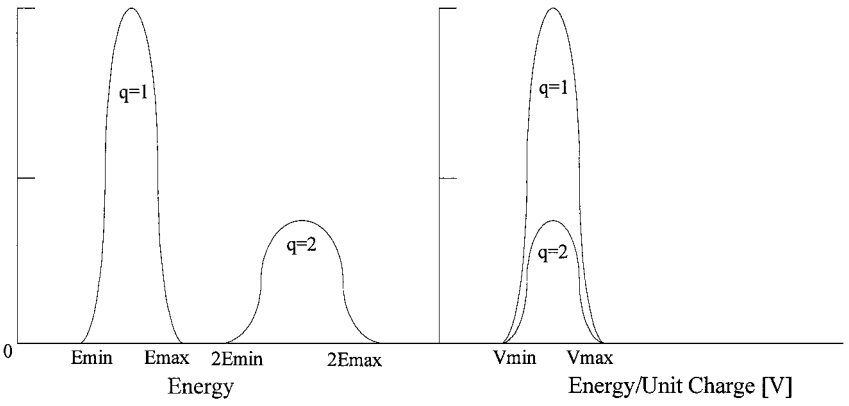

a) Precollision distributions

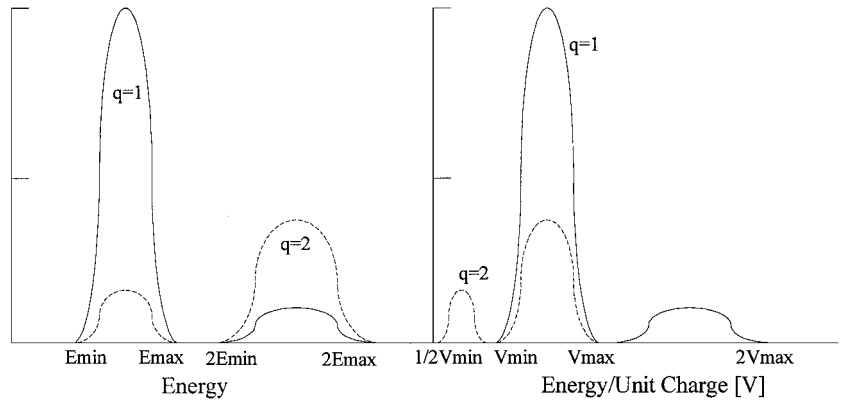

b) Postcollision distributions

Fig. 4 Effect of charge-exchange collisions on ion energy distribution functions (adapted from Ref. 26): singly and doubly charged ion distributions are $q = 1$ and $q = 2$, respectively.

will be accelerated to twice the kinetic energy of the singly charged ion created nearby. Barring collisions, the two particles would be registered by an RPA or the MBMS at the same E/q because the factor of two in energy of the doubly charged ion is canceled by the factor of two in charge. However, if along the path between the thruster and the probe the doubly charged ion should experience a charge exchange collision with the singly charged ion, there are three possible outcomes that are detectable by an analyzer. First, one electron is transferred from the singly charged ion to the doubly charged ion, resulting in a single ion with $E_i/q_i \sim 2V_i$ and a double ion with $E_i/q_i \sim 1/2V_i$. The precollision distribution and resulting postcollision distributions for this example are shown in Fig. 4. The second outcome will result in an electron being transferred from the doubly charged ion to the singly charged ion, resulting in a triply charged ion with $E_i/q_i \sim 2/3V_i$ and an undetectable neutral. The final possibility has two electrons transferred from the singly charged ion to the doubly charged ion, resulting in a triply charged ion with $E_i/q_i \sim 1/3V_i$ and an undetectable neutral. The detectable products for ion–ion charge exchange collisions are given in Table 3 for collisions involving singly, doubly, triply, and quadruply charged ions.[26]

A summary of the general traits of charge exchange collisions exhibited in ion energy data are shown in Fig. 4 and include[26] 1) appendages to the main distribution peak, which corresponds to the energy distribution of the colliding species; 2) auxiliary peaks that conserve the shape of the original distribution; 3) ion–neutral charge exchange collisions that produce ions that are detectable only at E/q ratios greater than the original ion E/q; and 4) ion–ion charge exchange collisions that can produce ions that are detectable at E/q ratios above and below the original ion E/q.

The effect of elastic collisions is to transfer momentum from doubly or triply charged ions accelerated in the discharge chamber to ions of lower charge state and neutrals because the former tend to move at a higher energy and, thus, overtake the latter. The signatures of elastic collisions and charge exchange collisions in energy analyzers are quite similar. Examples of the precollision and postcollision energy and E/q profiles are given in Fig. 5 for elastic collisions between singly and doubly charged ions. Because all ions experience the same accelerating voltage, the maximum E/q will be the same and close to the thruster discharge voltage. Thus, for doubly charged ions ($q = 2$ in Fig. 5) the high-voltage tail will decay to zero at approximately twice the discharge voltage. Although the minimum E/q is more difficult to define because it depends on the structure of the acceleration and ionization zones of the thruster, the peaks of the energy distributions for both singly and doubly charged ions will occur at the same E/q. The general traits of elastic collisions between an ion of charge $q = 1$ and an ion of charge $q = n$ that are present in ion energy data include[26] 1) a high-voltage tail on the singly charged ion E/q distribution that decays to zero at an E/q equal to n times the maximum precollision E/q of the charge n ion and 2) a low-voltage tail on the E/q distribution of the charge n ion that decays to zero at an E/q equal to $1/n$ times the minimum E/q of the singly charged ion.

Whereas there is little in the way of collision cross section data to support the theory presented, examination of MBMS ion energy data provides excellent validation of the model. Figure 6 shows MBMS data taken 1 m from the exit plane of the SPT-100. Overlaid in Fig. 6 are the individual ion energy profiles resulting from some of the ion–ion charge exchange collisions presented in Table 3. As Fig. 6 clearly shows, the MBMS profile exhibits signs of charges exchange collisions between singly, doubly, and triply charged ions. Thus, examination of the ion energy distribution can shed light on the ionization state emerging from the Hall thruster and, to an extent, the energetics involved in the ionization processes within the engine.

To strengthen this argument, time-of-flight (TOF) mass spectra data were obtained with the MBMS for the SPT-100. Figure 7 shows MBMS ion energy data with example mass spectra data taken at three E/q values of the profile. That triply charged xenon particles are not seen in the high-energy tail of the E/q distribution is expected because charge exchange collisions generate high-energy

Table 3 Ion–ion charge exchange collision products[26]

Reaction	Detectable product	Electrons transferred
$Xe^{2+} + Xe^{+}$	Xe^{+} at $E_i/q_i = 2V_i$ and Xe^{2+} at $E_i/q_i = 1/2V_i$	1
$Xe^{2+} + Xe^{+}$	Xe^{3+} at $E_i/q_i = 2/3V_i$	1
$Xe^{2+} + Xe^{+}$	Xe^{3+} at $E_i/q_i = 1/3V_i$	2
$Xe^{3+} + Xe^{+}$	Xe^{2+} at $E_i/q_i = 3/2V_i$ and Xe^{2+} at $E_i/q_i = 1/2V_i$	1
$Xe^{3+} + Xe^{+}$	Xe^{4+} at $E_i/q_i = 3/4V_i$	1
$Xe^{3+} + Xe^{+}$	Xe^{+} at $E_i/q_i = 3V_i$ and Xe^{3+} at $E_i/q_i = 1/3V_i$	2
$Xe^{3+} + Xe^{+}$	Xe^{4+} at $E_i/q_i = 1/4V_i$	3
$Xe^{3+} + Xe^{2+}$	Xe^{2+} at $E_i/q_i = 3/2V_i$ and Xe^{3+} at $E_i/q_i = 2/3V_i$	1
$Xe^{3+} + Xe^{2+}$	Xe^{+} at $E_i/q_i = 2V_i$ and Xe^{4+} at $E_i/q_i = 3/4V_i$	1
$Xe^{3+} + Xe^{2+}$	Xe^{+} at $E_i/q_i = 3V_i$ and Xe^{4+} at $E_i/q_i = 1/2V_i$	2
$Xe^{3+} + Xe^{2+}$	Xe^{5+} at $E_i/q_i = 3/5V_i$	2
$Xe^{3+} + Xe^{2+}$	Xe^{5+} at $E_i/q_i = 2/5V_i$	3
$Xe^{4+} + Xe^{+}$	Xe^{3+} at $E_i/q_i = 4/3V_i$ and Xe^{2+} at $E_i/q_i = 1/2V_i$	1
$Xe^{4+} + Xe^{+}$	Xe^{5+} at $E_i/q_i = 4/5V_i$	1
$Xe^{4+} + Xe^{+}$	Xe^{2+} at $E_i/q_i = 2V_i$ and Xe^{3+} at $E_i/q_i = 1/3V_i$	2
$Xe^{4+} + Xe^{+}$	Xe^{+} at $E_i/q_i = 4V_i$ and Xe^{4+} at $E_i/q_i = 1/4V_i$	3
$Xe^{4+} + Xe^{+}$	Xe^{5+} at $E_i/q_i = 1/5V_i$	4
$Xe^{4+} + Xe^{2+}$	Xe^{3+} at $E_i/q_i = 4/3V_i$ and Xe^{3+} at $E_i/q_i = 2/3V_i$	1
$Xe^{4+} + Xe^{2+}$	Xe^{+} at $E_i/q_i = 2V_i$ and Xe^{5+} at $E_i/q_i = 4/5V_i$	1
$Xe^{4+} + Xe^{2+}$	Xe^{2+} at $E_i/q_i = 2V_i$ and Xe^{4+} at $E_i/q_i = 1/2V_i$	2
$Xe^{4+} + Xe^{2+}$	Xe^{6+} at $E_i/q_i = 2/3V_i$	2
$Xe^{4+} + Xe^{2+}$	Xe^{+} at $E_i/q_i = 4V_i$ and Xe^{5+} at $E_i/q_i = 2/5V_i$	3
$Xe^{4+} + Xe^{2+}$	Xe^{6+} at $E_i/q_i = 1/3V_i$	4
$Xe^{4+} + Xe^{3+}$	Xe^{3+} at $E_i/q_i = 4/3V_i$ and Xe^{4+} at $E_i/q_i = 3/4V_i$	1
$Xe^{4+} + Xe^{3+}$	Xe^{2+} at $E_i/q_i = 3/2V_i$ and Xe^{5+} at $E_i/q_i = 4/5V_i$	1
$Xe^{4+} + Xe^{3+}$	Xe^{2+} at $E_i/q_i = 2V_i$ and Xe^{5+} at $E_i/q_i = 3/5V_i$	2
$Xe^{4+} + Xe^{3+}$	Xe^{+} at $E_i/q_i = 3V_i$ and Xe^{6+} at $E_i/q_i = 2/3V_i$	2
$Xe^{4+} + Xe^{3+}$	Xe^{+} at $E_i/q_i = 4V_i$ and Xe^{6+} at $E_i/q_i = 1/2V_i$	3
$Xe^{4+} + Xe^{3+}$	Xe^{7+} at $E_i/q_i = 4/7V_i$	3
$Xe^{4+} + Xe^{3+}$	Xe^{7+} at $E_i/q_i = 3/7V_i$	4

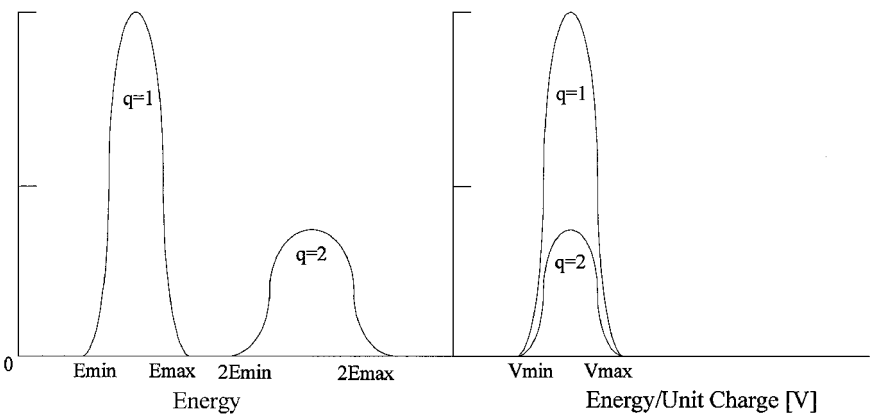

a) Precollision distributions

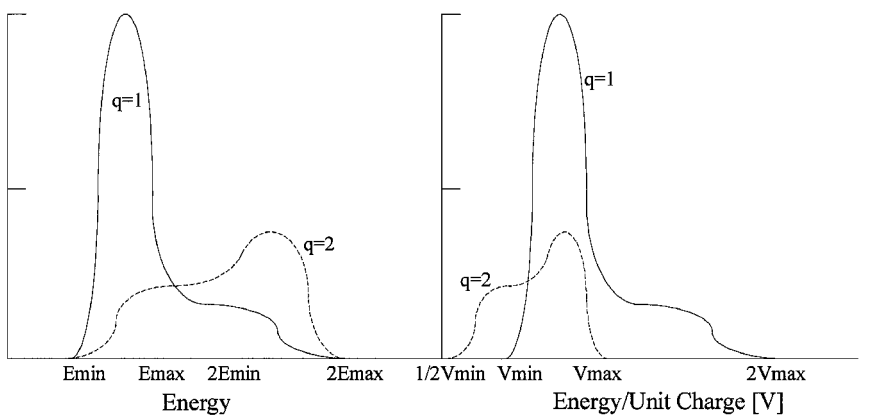

b) Postcollision distributions

Fig. 5 Effect of elastic collisions on ion energy distribution functions (adapted from Ref. 26): singly and doubly charged ion distributions are $q = 1$ and $q = 2$, respectively.

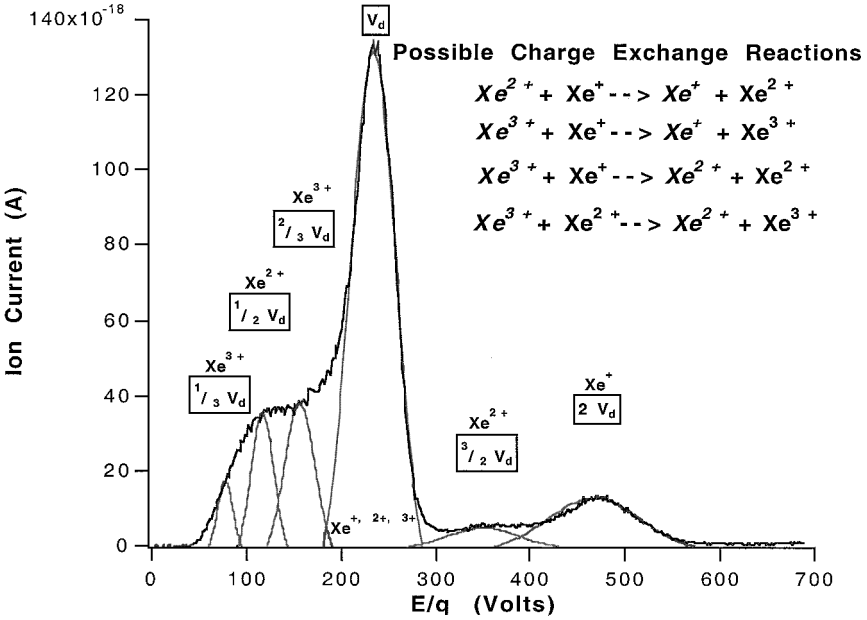

Fig. 6 Example MBMS data showing charge exchange collision signatures in ion energy data taken 1 m from the thruster exit plane; high-energy reactants and products of the charge exchange collisions in italics.

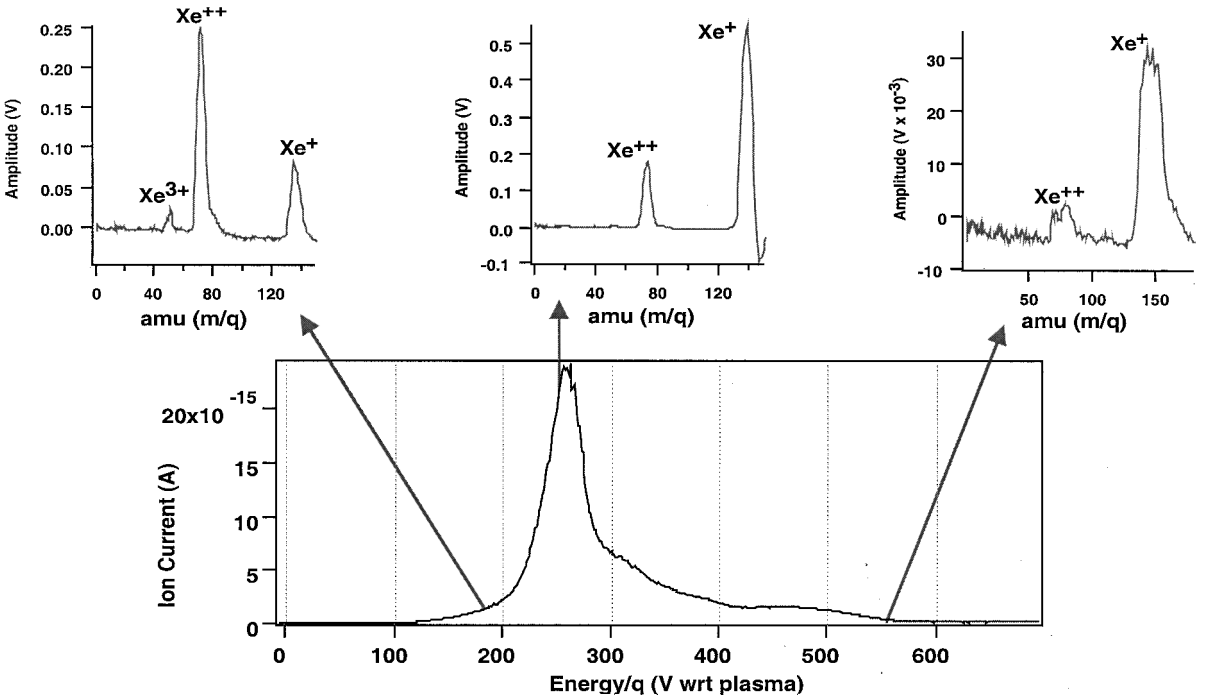

Fig. 7 Example MBMS data showing ionization state as a function of *E/q* 1 m from the thruster exit plane.

tail particles while reducing the population of higher charge states. However, the absence of triply charged ions near the peak E/q of the distribution may lead one to suggest that these ions are created in a multistep process and are, thus, not accelerated to the same acceleration potential. Although this may be true, the most probable voltage (E/q) for triply ionized xenon was measured to be only 20 V less than the most-probable voltage for singly charged ion (255 V vs 274 V) 0.5 m from the thruster.[15] Thus, the lack of triply charged xenon ions near the peak E/q for the 1-m data can be attributed to charge exchange collisions in the extra half-meter of the plume because this process tends to reduce the overall charge state of the plasma.

Although the ion energy distribution data obtained with the MBMS provided much insight on collisional processes occurring within the SPT-100 plume, this instrument could not distinguish the ion energy distributions of different ion species directly without its TOF mass differentiating capability because different ion species that have experienced an identical (or similar) acceleration voltage would appear at the same (or similar) voltage in the distribution. However, this time-consuming method of obtaining energy distributions for various ion species resulted in a somewhat poor voltage resolution because the ion mass spectra were acquired for voltages in 10-V intervals.[23] To this end, an $\boldsymbol{E} \times \boldsymbol{B}$ probe was employed to measure the ion energy distribution of singly and multiply charged plume ions directly and with better voltage resolution. Because an $\boldsymbol{E} \times \boldsymbol{B}$ probe separates different ion species according to their velocities, as opposed to RPAs and the MBMS that are sensitive only to E/q, the probe acts as a velocity filter. It can been shown in the derivation of the $\boldsymbol{E} \times \boldsymbol{B}$ probe governing equations that the filtered velocity is independent of the mass or charge state of the analyzed particle.[23] Thus, the $\boldsymbol{E} \times \boldsymbol{B}$ probe will provide the ion energy distribution function of ions of a variety of charge states that reach

the detector whole, that is, in the charge state they left the thruster, and that have been transformed into another charge state through charge exchange collisions. In either case, the $\boldsymbol{E} \times \boldsymbol{B}$ probe provides a great deal of information on the distribution of upper charge state ions emerging from the thruster because charge exchange collisions result in a negligible change in particle momentum.

To glean ion energy distribution function information out of $\boldsymbol{E} \times \boldsymbol{B}$ probe data, probe current vs energy traces were curve fit to ion energy distribution curves [Eq. (1)] for each ion charge state:

$$I_i(E_i) = K_0 + K_1 \cdot E_i \cdot \exp\left[-\beta \cdot \left(\left|\sqrt{E_i} - \sqrt{E_b}\right|\right)^n\right] \quad (1)$$

Equation (1) is related to the basic distribution function

$$f(E_i) = K \cdot E_i^{\frac{1}{2}} \cdot \exp\left(-\beta \cdot E_i^{n/2}\right) \quad (2)$$

through some curve-fitting constants (K_0, K_1, β, E_b, and n) and an elementary Galilean transformation to take into account the convecting ion beam.[23] A Maxwellian distribution corresponds to an n value of 2, whereas a Druyvesteyn distribution, another well-known distribution function, corresponds to an n value of 4. An example of a Druyvesteyn distribution is a steady ion beam immersed within a uniform steady electric field undergoing only elastic collisions with neutral gas atoms.[27] A similar set of equations and approach have been employed by others to model successfully the electron energy distribution function.[28,29] Details of the curve-fitting procedure may be found in Ref 23.

Figure 8 shows a typical fit of Eq. (1) to $\boldsymbol{E} \times \boldsymbol{B}$ probe data and demonstrates that the model produced a fitted curve with an n value of 3.3 that agreed very well with the measured probe trace. Notice that this n value lies between 2 and 4, the values for a Maxwellian distribution and a Druyvesteyn distribution, respectively.

Figure 8 also shows that the model deviates from the measured data at low- and high-energy ranges, as can be seen more clearly in Fig. 9, which shows the measured probe trace and the sum of the fitted curves of singly, doubly, triply, and possibly quadruply charged (Xe^{1+}, Xe^{2+}, Xe^{3+}, and Xe^{4+}, respectively) ions. The comparison of the experimental data with the curve fit shows exceptional agreement in the upper portion of the peaks. However, the curve fits do not agree with the experimental data at low energy (~200 eV) and in the regions between the peaks. The disagreement at low energy ($E_i < 220$ eV) may be due to significant ion production near the exit plane of the thruster, which results in low-energy ions. It may also be due to charge exchange collisions with neutral atoms that

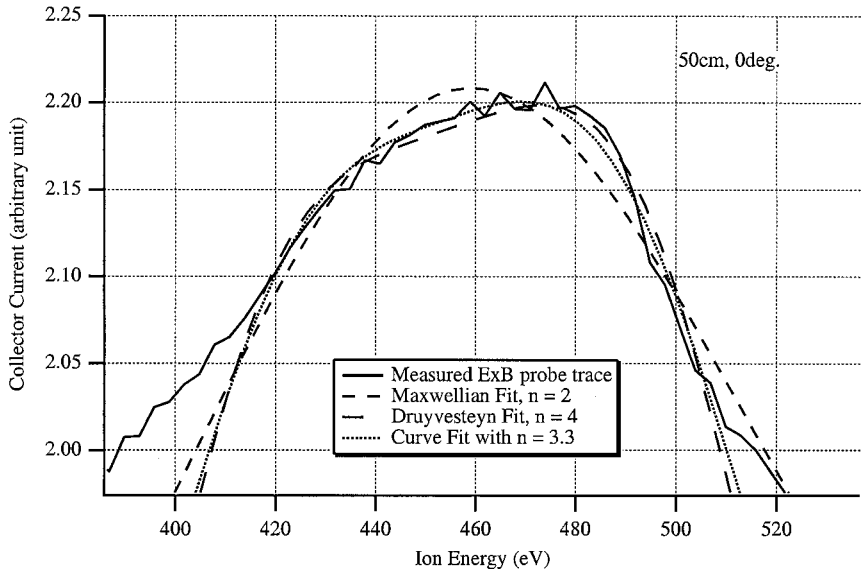

Fig. 8 Comparisons between the Maxwellian ($n = 2$) and Druyvesteyn ($n = 4$) curve fits and the $E \times B$ probe trace ($n = 3.3$) of Xe^{2+} ion peak measured on the thruster axis 50 cm from the thruster exit (from Ref. 23).

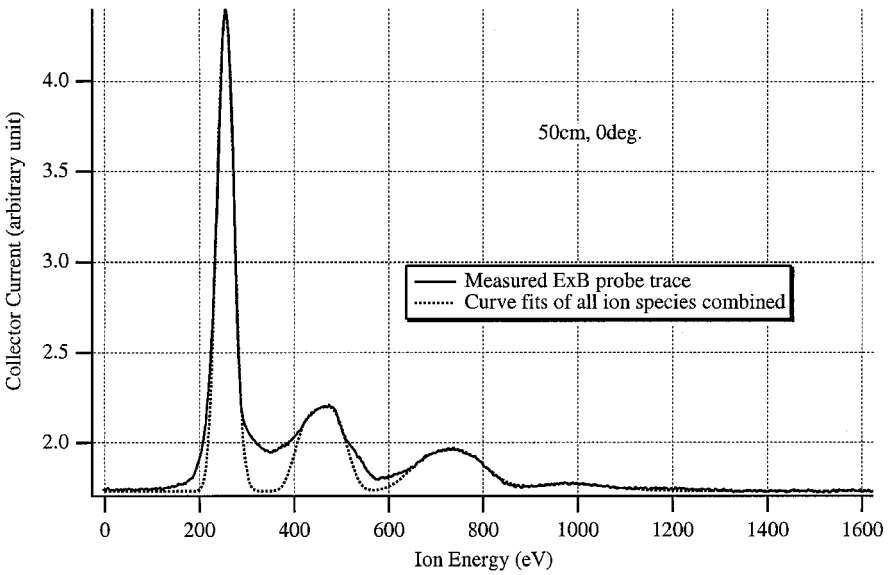

Fig. 9 SPT-100 $E \times B$ energy trace and curve fits to each charge state measured on the thruster axis at 50 cm from the thruster exit. Sum of the curve fits of Eq. (1) for Xe^{1+}, Xe^{2+}, Xe^{3+}, and possibly Xe^{4+} ion peaks (such as shown in Fig. 8) overlaid on the $E \times B$ probe trace (from Ref. 23).

would create a population of low-energy ions that would fall outside of the Maxwellian or Druyvesteyn models. The disagreement in the regions between the peaks is most likely attributed to elastic collisions between the particles of the two ion species that the peaks represent. The effect of elastic collisions manifests itself in the probe trace as highly overlapped regions between the peaks representing the two ion species.[15,26] For example, the overlapped region between the first peak (representing Xe^{1+} ions) and the second peak (representing Xe^{2+} ions) is the result of elastic collisions between Xe^{1+} ions and Xe^{2+} ions. Then, the fitted curves can be thought to represent the precollision distributions. As such, the peak height of the fitted curve must be lower than the true precollision distribution function because the population of ions that have undergone elastic collisions shifts toward the region between the peaks. The model would be improved if it were incorporated with a scheme for predicting elastic collisions. Such a scheme requires collision cross section data involving multiply charged xenon ions, which have not been found in the literature. However, it is evident, from the excellent agreement shown in the upper part of the peaks, that this simple model can produce precollision distribution functions very well.

The ion species fractions were calculated determining the first moment of the distribution functions derived from the curve fits for each ion species, that is, number density n_i, and calculating the corresponding fractions of each species.[23] Comparison between $\boldsymbol{E} \times \boldsymbol{B}$ probe-measured ion species fractions with values obtained by King[15] with the MBMS by comparing relative peak heights in the mass spectra data for each species is shown in Table 4. Emission spectroscopic data taken by Manzella[12] are also presented for comparison. Given the small field of view of the $\boldsymbol{E} \times \boldsymbol{B}$ probe and MBMS, caution must be exercised in extrapolating charge state fractions calculated from these devices to the entire plume. However, because the optical measurements were collected from an 80-mm (radial) × 0.08-mm (axial) cross section at the exit of the thruster, the optical data of Table 4 can be thought of as being representative of the entire plume. The uncertainty for the $\boldsymbol{E} \times \boldsymbol{B}$ probe, MBMS, and optical techniques are ±8, ±5, and ±20%, respectively.[12,15,23] Both $\boldsymbol{E} \times \boldsymbol{B}$ probe and MBMS data show that a nontrivial fraction of the ion beam is composed of multiply charged xenon ions. This must be accounted for if accurate models to predict thruster and spacecraft surface erosion rates are to be developed. Whereas there is no reason to suggest that any of these techniques are more accurate than the others, the disagreement between the $\boldsymbol{E} \times \boldsymbol{B}$ probe data and the other two data sets may be attributed to the underestimation of the Xe^{1+} ion fraction due to the curve-fit limitations discussed before and exhibited in Fig. 9. Xe^{4+} may have been detected by the $\boldsymbol{E} \times \boldsymbol{B}$ probe (Fig. 9) but the signal-to-noise ratio was too low to rule out other species. However, the other candidate species (singly ionized N_2 and O_2) are somewhat unlikely because they would most likely become dissociated before being ionized.

Table 4 Comparison between $E \times B$ probe-measured ion species fractions with values obtained by King[15] (MBMS) and Manzella[12] (optical)

	$\boldsymbol{E} \times \boldsymbol{B}$ probe	MBMS	Optical
Xe^{+}	0.79	0.89	0.89
Xe^{2+}	0.16	0.11	0.119
Xe^{3+}	0.05	0.002	——

Figure 10 shows the variation of the n value for the corresponding ion energy curve fits of $\boldsymbol{E} \times \boldsymbol{B}$ probe data with respect to angle off thruster axis at 1 m from the thruster exit. Positive angles represent data collected on the cathode side of the thruster. Figure 10 shows that most of the ion species distribution functions lie somewhere between a Maxwellian ($n = 2$) and a Druyvesteyn ($n = 4$) distribution. Note that the distribution functions for Xe^{1+} ions are closer to a Maxwellian distribution than those for other ion species. Similar results were observed with n value data taken 50 cm from the thruster exit plane. That the Xe^{1+} ions are closer to Maxwellian is not surprising because a Maxwellian distribution represents a group of particles in equilibrium where the equilibrium state is achieved by collisions among the particles. Because the ion–ion elastic collision frequency increases with increasing number density,[23] and because the ion beam of the SPT-100 is composed mostly of Xe^{1+} ions (Table 4), these ions are expected to undergo more elastic collisions as a group than higher charge state xenon ions do.

The (most probable) beam energy E_b was calculated for each ionization state of xenon as a biproduct of fitting $\boldsymbol{E} \times \boldsymbol{B}$ data to Eq. (1). Figure 11 shows the beam energy per charge of the ion species 1 m from the thruster exit. Given the large error bars and the erratic and asymmetrical nature of the data, it is difficult to glean trends from Fig. 11 except that E_b/q for Xe^{1+} ions was almost always the highest. It has been shown that the electron temperature in SPT discharge chambers attains a maximum in the region of highest magnetic field strength, which occurs very near the thruster exit.[30] Because the ionization potential increases with ionization charge state, it is expected that the formation of multiply charged ions from electron-impaction ionization of neutrals will tend to occur more toward the exit of the discharge chamber. Moreover, some of the multiply charged ions may be created from a multistep ionization process, which would also cause them to experience less of the acceleration voltage. However, that E_b/q for Xe^{2+} ions was almost always lower than those of Xe^{3+} ions contradicts the ionization mechanism discussed earlier. Hence, the formation and acceleration of multiply charged ions must be significantly more complicated than the simple phenomenological model given earlier. Processes such as ion

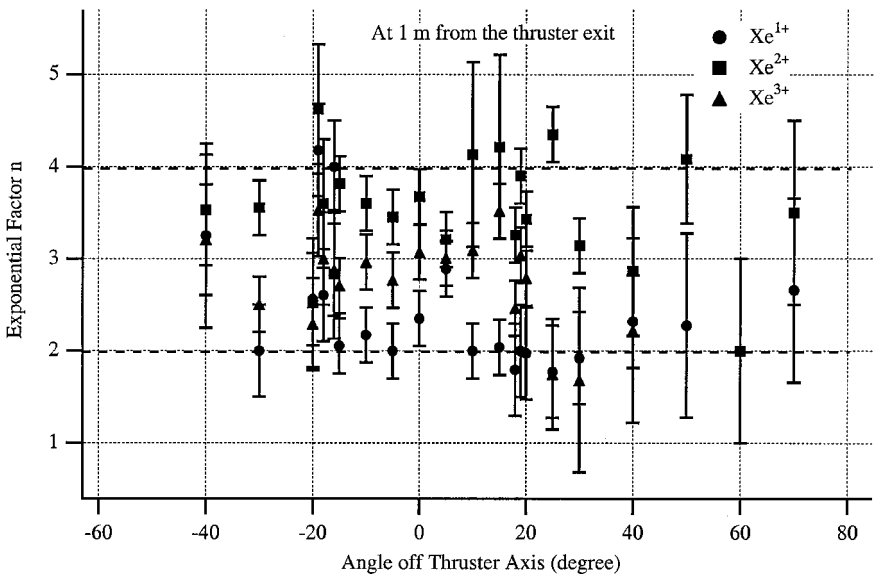

Fig. 10 Exponential factor n in Eq. (1) obtained from the curve fits of the $E \times B$ probe data at 1 m from the thruster exit (from Ref. 23).

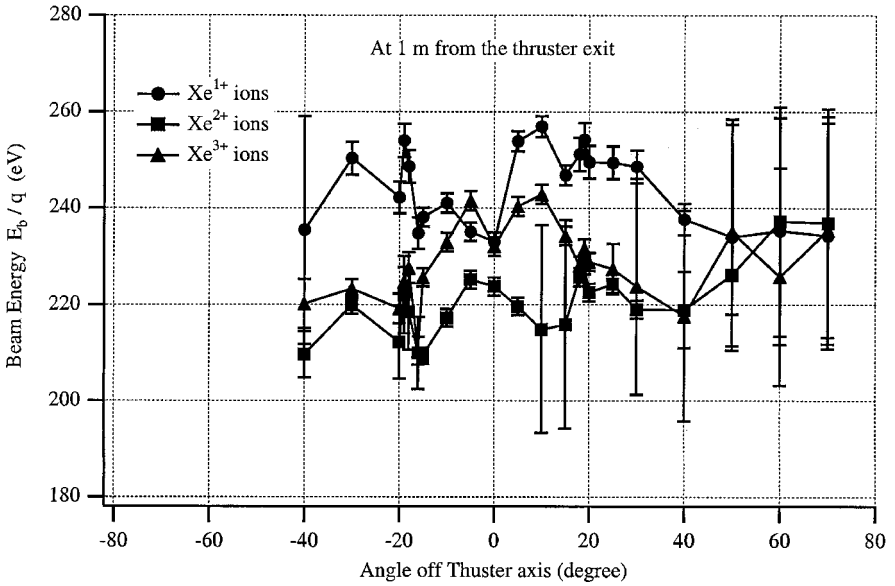

Fig. 11 Most probable beam energy per charge of Xe^{1+}, Xe^{2+}, and Xe^{3+} ions obtained from the curve fits of the $E \times B$ probe data at 1 m from the thruster exit (from Ref. 23).

collisions with the chamber wall, subsequent ionization, and charge exchange collisions may convolute the physics. Clearly a great deal more work must be done before a more clear understanding of these processes is at hand.

Facility Effects

One of the major concerns that any electric propulsion plume researcher must contend with is facility effects. Because the dimensions of the LVTF are much larger than the distance from where the thruster plume data were collected, chamber wall effects were not considered critical. What was of more concern was the tank pressure.

Randolph et al.[31] suggest that to characterize a CDT in terms of far-field (greater than ~1 m) plume properties, the vacuum chamber pressure should be no more than 1.6×10^{-3} Pa (1.2×10^{-5} torr). This is a factor of four lower than the pressure maintained in the LVTF during the SPT-100 tests reported earlier. Because the pressure at low Earth orbit and at geosynchronous orbit are approximately 7×10^{-4} and 7×10^{-8} Pa, respectively, a perfect simulation of pressure is not always necessary. Randolph et al. based their analysis on free-molecular flow, arguing that, below a certain chamber pressure, thruster operating characteristics are not affected by the random flux of vacuum chamber background particles into the discharge chamber or plume. Conversely, if a thruster is tested above the specified pressure, the influence of background gas being ingested into the engine through free-molecular flow must be taken into account when analyzing test data. Further, a large partial pressure of background gas molecules can affect ion current density and energy distribution measurements by artificially increasing the local charge density through charge exchange collisions. For example, at large angles from the thruster axis, the ion energy distribution profile is dominated by low-energy charge exchange ions, the source of which is thought to be background gas.[25] Although no attempts to correct for facility pressure effects were made with the SPT-100 data presented here, we were able to investigate the role of facility pressure on far-field plume data through a rather straightforward means: We repeated some of the tests, albeit with a different thruster, at an order of magnitude lower tank pressure. Results of these tests will be the focus of the next section.

Near-Field and Far-Field Experiments with the P5

LVTF Modifications

One of goals of the experiments to be presented in this section was to evaluate the role of tank pressure on ion energy distribution and charge state measurements. In 1998, the LVTF underwent a major pumping system upgrade. The diffusion pumps were capped off and replaced by a pumping system consisting of four CVI model TM-1200 internal cryopumps (Fig. 2). The mechanical and blower pumping train described in the preceding section is used to evacuate the chamber to less than 10 Pa so that the cryopumps can be activated. These internal cryopumps are similar to the popular 1.2-m-diam CVI TM-1200 cryotubs except that they are placed within the chamber and, hence, provide roughly twice the pumping speed of a cryotub. The four cryopumps provided a measured xenon pumping speed of 140,000 l/s and an ultimate base pressure of less than 3×10^{-5} Pa (2×10^{-7} torr). Pressure was determined by averaging the measurements of two ion gauges: a Varian model 571 gauge with an HPS model 919 controller and a Varian model UHV-24 nude gauge with a Varian senTorr controller. The nude gauge, senTorr controller, and connecting cable were calibrated as a unit on nitrogen by the manufacturer. A calibration factor of 2.87 was used to convert indicated (nitrogen) pressure to xenon pressure.[32] The operating tank pressure corrected for xenon for this experiment was 7.3×10^{-4} Pa (5.5×10^{-6} torr) for a thruster discharge current of 5.4 A. A 1.8 by 1.8 m louvered graphite beam dump was installed in the middle of the endcap that is downstream of the thruster to minimize sputtering of chamber wall material. All other aspects of the facility are as described in the preceding section.

Table 5 Mean free paths (MFP) for 7.3×10^{-4} Pa (5.5×10^{-6} torr) tank pressure

Collision	Chamber MFP, m
Xe^{+} + Xe charge exchange	11.1
Xe^{2+} + Xe charge exchange	8.1
Electron–electron elastic	5.1
Electron–ion elastic	4.9
Ion–ion elastic	1.2
Ion–electron elastic	6.4
Ion–neutral elastic	95.7
Electron–neutral elastic	29.1
Neutral–neutral elastic	12.7

The pressure maintained in the tests described in this section fulfilled the criterion established by Randolph et al.[31] Some mean free path estimates, which correspond to the new operating pressure of the LVTF, are given in Table 5. At this chamber pressure, the background neutral number density is approximately 2×10^{17} m^{-3} vs 8×10^{18} m^{-3} at the exit plane of the P5. Note that the chamber-induced charge exchange mean free paths are significantly larger than the distance over which measurements were taken (0.75 m). Over 90% of the beam ions are predicted to travel 1 m without

experiencing a charge exchange collision with background chamber gas particles. Thus, the vast majority of charge exchange collisions observed are due to interactions between particles that emanate directly from the thruster, that is, not with background chamber gas particles. As such, the results obtained in these experiments are expected to be indicative of those that would be obtained in space.

P5 Hall Thruster

Because the SPT-100 was unfortunately no longer available for this phase of testing, another Hall thruster was needed. The thruster used for this investigation was the University of Michigan/U.S. Air Force Research Laboratory P5 5-kW laboratory-model stationary plasma thruster. This thruster was developed specifically for diagnostic access to the discharge chamber and yet to posses performance and plume divergence characteristics commensurate with commercial engines. Compared to smaller thrusters, such as the SPT-100, the P5 provides a larger discharge chamber for better spatial resolution for electrostatic probes, as well as a lower power density to reduce the heat flux to the probes.

The P5 used an impregnated tungsten hollow cathode provided by NASA GRC and later a lanthanum hexaboride (LaB6) cathode provided by the Moscow Aviation Institute. The operating characteristics of the thruster on either cathode were identical. Thrust, specific impulse, and efficiency have been characterized thoroughly and have been reported, along with plasma parameter profiles in the plume, in a previous work.[9] The P5's performance and plume characteristics are similar to a number of 5-kW-class commercial engines. As such, the results obtained with the P5 should be similar to those that would have been obtained had a commercial SPT been tested.

MBMS Modifications for Near-Field Measurements

The configuration of the MBMS was not changed for far-field plume measurements (50 and 75 cm). However, a low cross section 67-cm-long extension was placed on the MBMS for near-field measurements (10 cm) to minimize the buildup of the neutral ram cloud and to protect the thruster from deposition of backsputtered material. The near-field skimmer was constructed from off-the-shelf vacuum components that necked down as they neared the thruster. The first section of the extension (closest to the gate valve) had an outer diameter of 6.35 cm. A Varian Model V70LP turbomolecular pump was used to evacuate this section. The water-cooled turbomolecular pump, rated at 68 l/s on nitrogen, used the LVTF itself as a backing pump and lowered the pressure within this section by a factor of 15 to the 10^{-5}-Pa range. The next two components, including a flexible coupling, had an outer diameter of 3.81 cm. The flexible coupling was installed to facilitate alignment of the sampling orifice with the entrance slit to the 45-deg energy analyzer and to maintain alignment during endcap contraction as the LVTF is evacuated. The sampling skimmer was fixed with respect to the thruster using an optics mounting post, and the flexible coupling took up the displacement of the endcap. The final section of hardware (closest to the thruster) was 1.91 cm in diameter and contained a porcelain sampling skimmer with an orifice approximately 6.9 mm in diameter. Unlike the far-field measurements, which used the center of the thruster as the axis of symmetry, all angles reported for near-field measurements are respect to the center of the annular discharge chamber.

P5 Results

Figure 12 shows far-field ion energy data taken along thruster centerline some 75 cm from the thruster exit plane at an operating condition of 5.3 A at 300 V. This condition was selected to mimic the engine behavior of the SPT-100, which was at 4.5 A at 300 V. Figure 12 shows that the primary ion energy distribution has its peak at 263 V with respect to ground. For this condition, the plasma potential was approximately 8 V above ground.[26] The peak is at 88% of the discharge voltage, which is what is expected for a well-developed Hall thruster. We see structure in the primary peak that provides strong evidence of elastic collisions between singly and doubly charged ions. This behavior is very similar to that observed and presented for the SPT-100 earlier. When this distribution is examined more closely on a semilog plot (Fig. 12b), we see evidence of small charge exchange collision peaks at two and three times the primary peak. Because there are no charge exchange peaks at voltages less than the primary peak, these additional peaks are due to high-energy singly charge ions that result from charge exchange collisions between doubly and triply ionized xenon and neutrals (refer to Table 3).

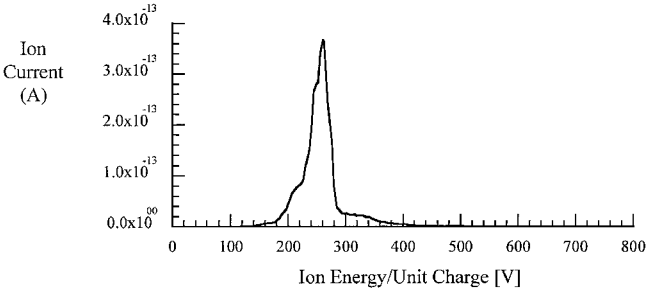

a) Linear

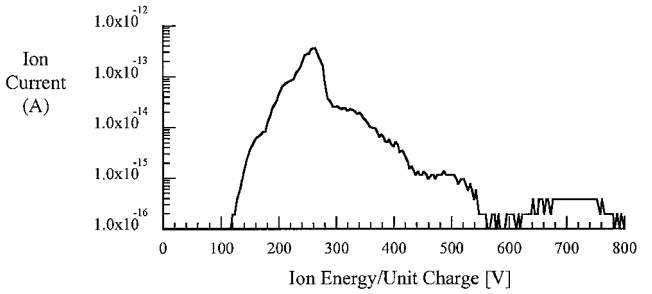

b) Semilog

Fig. 12 Ion energy data taken 75 cm from exit plane and at 0 deg at a thruster condition of 5.3 A–300 V in both linear and semilog format (from Ref. 26).

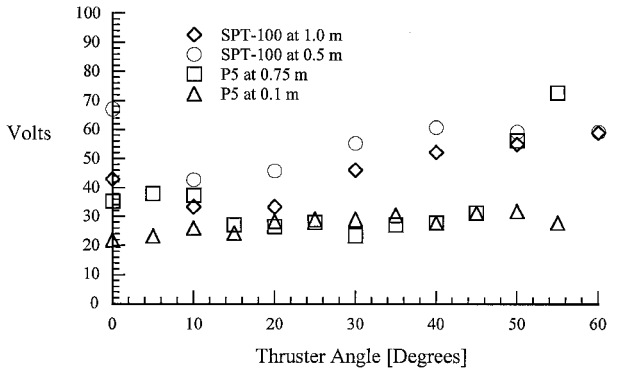

Fig. 13 FWHM of the primary ion energy peak for the P5 at 5.3 A–300 V and the SPT-100 at 4.5 A–300 V (from Ref. 26). Uncertainty is ± 1 V.

Whereas the trends observed in the far-field P5 data are similar to those obtained with the SPT-100 at a much higher chamber pressure, one of the telltale signs of an ion energy distribution that has been affected by chamber-induced collisional effects is the broadening of the energy peaks.[15] To this end, a figure of merit for identifying facility pressure effects in ion energy data is the full width at half-maximum (FWHM) of the primary energy peak. FWHM data of the primary ion energy peak for both the P5 and the SPT-100 as a function of angle off thruster centerline are presented in Fig. 13. The narrower ion energy profiles of the P5 compared to those measured with the SPT-100 may be indicative of the better chamber pressure. With lower background pressure, the frequency of pressure-broadening collisions is reduced, and thus, the profiles are narrower.

We see that the FWHM data are broadened in the far field at high angles and along and near centerline for the SPT-100 data set. Although the same trend is observed for the P5 FWHM profiles

taken 75 cm from the exit plane, albeit to a much lower extent, the 10-cm profile is almost flat, exhibiting only a slight increase at moderate angles. Whereas we cannot rule out that these differences may be because these data were collected on two different engines, these observations can also be explained as follows.

At high angles (>45 deg), a significant portion of the ion current is composed of low-energy charge exchange ions because the dominant portion of the ion beam is contained within a cone of half-angle 45 deg (Ref. 25). Additionally, many of the low-energy ions that emanate from the downstream region of the discharge chamber tend to be directed inward, that is, toward thruster centerline, due to the convex magnetic and electric fields in this zone.[33] Many of these low-energy ions then cross over the centerline of the thruster and collide with particles emanating from the discharge chamber on the opposite side of the thruster. These collisions may cause the ion energy distribution function broadening that is seen.

At low angles, the conjecture is that when the thruster is firing directly toward the sampling skimmer, ions from the thruster that do not enter the orifice impact the surrounding flange and are neutralized, thereby creating a localized area of higher pressure neutral xenon that would cause collisions and a broader profile.[15]

This hypothesis was checked by placing a neutral particle flux (NPF) probe just below the sampling orifice of the far-field MBMS configuration, perpendicular to the flow. The NPF probe is a combination RPA and hot cathode ion gauge.[34] The NPF probe grids were charged to repel all ions and electrons, and the ion gauge was used to obtain pressure changes relative to the background pressure measured by another ion gauge as the thruster was rotated. There was excellent agreement between the gauges at angles above 30 deg. There was a notable increase in pressure, however, within 20 deg of centerline, the same region where the far-field FWHM measurements show broadening. A 35% increase in pressure (from 7.3 to 9.8 $\times$ 10^{-4} Pa) was measured as the thruster was rotated to 0 deg with respect to the probe axis.[26] This measured higher pressure would increase the singly to doubly charged charge exchange collision probability only from 7 to 9% at 75 cm. This test was done only for the MBMS configured for far-field measurements because the entrance extension placed on the MBMS for near-field measurements should have ameliorated this situation.

Figure 14 shows ion energy data taken along the discharge chamber centerline 10 cm from the thruster exit plane at an operating condition of 5.3 A at 300 V. First we notice that the trace taken at 10 cm is significantly narrower than that taken at 75 cm (Fig. 12). The FWHM in the near field was 22 V, as compared to 35 V in

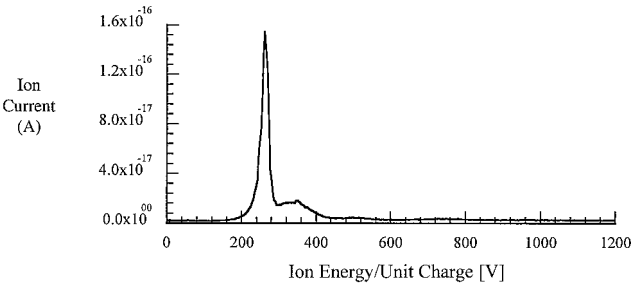

a) Linear

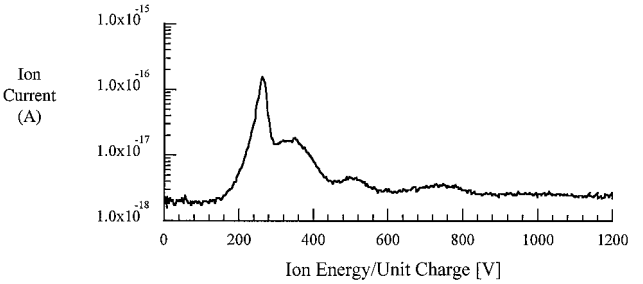

b) Semilog

Fig. 14 Ion energy data taken 10 cm from exit plane at a thruster condition of 5.3 A–300 V in both linear and semilog format (from Ref. 26).

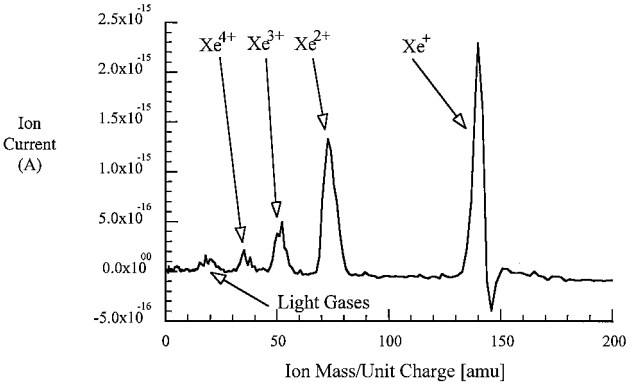

a) TOF mass spectra data 10 cm, centerline

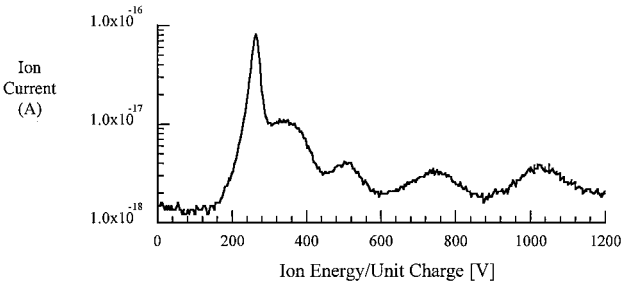

b) Ion energy 10 cm, 5 deg (semilog)

Fig. 15 Near-field MBMS mass spectra data for an *E/q* = 263 V at the discharge chamber centerline at a thruster condition of 5.3 A–300 V (from Ref. 26).

the far field. The increased width appears to be from low-energy elastic collisions. We also see that the somewhat distinct 1.33 times charge exchange collision peak observed at 10 cm has disappeared by 75 cm. In general, elastic collisions are far more prevalent in the far field than in the near field, obscuring charge exchange collision peaks in some cases. This is as expected because charge exchange collisions are approximately an order of magnitude more likely than elastic collisions for Hall thruster plasmas. Thus, by sampling close to the thruster, plume ions are interrogated before they have had an opportunity to undergo a significant number of elastic collisions.

Figure 15a shows near-field TOF mass spectra data taken 10 cm from the thruster exit plane along the center of the discharge chamber. These data were collected for the most probable ion energy for this condition, 263 V. In addition to the singly, doubly, and triply charged xenon, all of which were detected in the far field, we observe the presence of a peak at 32 AMU, which could correspond to two different species: quadruply ionized xenon or ionized oxygen molecules. However, some of the near-field ion energy measurements (e.g., Fig. 15b) detected charge exchange peaks at 1.33 and 4 times the primary discharge peak energy, which correspond to quadruply ionized xenon that is accelerated close to the beam voltage of the thruster.[26] Additionally, O_2^+ is expected to be very uncommon because it would have to survive being ingested, ionized, and accelerated by the thruster without dissociating. Moreover, it would most likely be ionized near the exit of the thruster, where the electron temperature is highest, and therefore not be accelerated to near the beam voltage. Note no evidence for Xe^{4+} is seen in any of the far-field data. Collisions that remove quadruply ionized xenon from the system are greater in number and probability than those that produce it. As such, by the time a sample is taken 75 cm from the thruster, almost all of the quadruply charged xenon has been converted to lower charge state ions or neutrals, increasing the fraction of these other ion species in the process.

Table 6 presents the overall ion species fraction taken with the MBMS for the P5 at 10 and 75 cm from the exit plane. The uncertainty of the MBMS data is $\pm$5%. We see that the far-field species fractions of the P5 are in line with those measured for the SPT-100. We also notice, however, that the fraction of multiply charged ions in the near field is much greater than those in the far field. Thus, while the thruster is actually producing a fair number of multiply charged

Table 6 Overall near- and far-field ion species fractions measured with the MBMS for the P5 operating at 5.3 A–300 V

Species	10 cm	75 cm
Xe^{+}	0.698	0.925
Xe^{2+}	0.231	0.068
Xe^{3+}	0.052	0.007
Xe^{4+}	0.019	——

ions, collisions within the plume reduce the overall charge state of the plasma. Note, however, that although the charge state of the plume is reduced through charge exchange collisions the propensity of the plume to sputter damage spacecraft surfaces will not diminish given the negligible impact on speed and trajectory these collisions have on participating particles.

Conclusions

A comprehensive investigation of Hall thruster plume plasma ion energy distribution functions and ion charge state has been made on both flight- and laboratory-model engines. This investigation was facilitated by the use of the MBMS energy analyzer/mass spectrometer and an $\boldsymbol{E} \times \boldsymbol{B}$ probe. The results of this investigation show that the Hall thruster plume is more energetic than previously thought. The plume contains a significant amount of energetic, multiply charged particles, whose energy distribution functions exhibit both Maxwellian and Druyvesteyn traits. Detection of these multiply charged ions by energy analyzers has been hampered in the past by charge exchange and elastic collisions. The high-energy tail seen in numerous energy analyzer data is thought to result from charge exchange and elastic collisions between singly and multiply charged ions and neutrals. To this end, charge exchange collisions provided the first indications that the Hall thruster plume is composed of multiply charged ions. The energy distribution and charge state of the beam ions must be accounted for properly in modeling the erosion rate of solar array cover glass and interconnect material. Otherwise, a severe underprediction of erosion rate may ensue. The role of facility pressure was also investigated and was found to have an influence mainly on the width of the ion energy distribution function. This pressure broadening is caused by elastic collisions between beam ions and background chamber gas particles.

Acknowledgments

This work was supported by the following grants from the Air Force Office of Scientific Research: F49620-95-1-0331, F49620-91-1-0107, and F49620-98-1-0033. Mitat Birkan was the Contract Monitor for all of these grants. The author wishes to acknowledge the former graduate students who performed the experiments presented: Frank Gulczinski III, Sang-Wook Kim, and Lyon B. King. The author wishes to thank Michael Day of Space Systems/Loral for providing the SPT-100 and power processing unit, the U.S. Air Force Research Laboratory for building the P5, and graduate student James Haas, who was instrumental in designing the P5. The author also wishes to acknowledge the support of the departmental technical staff and his graduate students at the Plasmadynamics and Electric Propulsion Laboratory in assisting on maintaining the facilities and experiments.

References

[1]Deininger, W. D., "Advanced Propulsion System Options for Geostationary Satellites," AIAA Paper 94-3001, June 1994.

[2]Sutton, G. P., *Rocket Propulsion Elements*, 6th ed., Wiley, New York, 1992, pp. 36–38.

[3]Kaufman, H. R., "Technology of Closed-Drift Thrusters," AIAA Paper 83-1398, June 1983.

[4]Brown, C. O., and Pinsley, E. A., "Further Experimental Investigations of a Cesium Hall-Current Accelerator," *AIAA Journal*, Vol. 3, No. 5, 1965, pp. 853–859.

[5]Chubb, D. L., and Seikel, G. R., "Basic Studies of a Low Density Hall Current Ion Accelerator," NASA TN D-3250, Feb. 1966.

[6]Kaufman, H. R., Robinson, R. S., Day, M. S., and Haag, T. W., "End-Hall Thrusters," AIAA Paper 90-2595, July 1990.

[7]Burgrova, A. I., Yermakov, Y. A., Morozov, A. I., and Yakunin, S. A., "A New Stage of Stationary Plasma Engine (SPE) Development," Anniversary Specialist Conf. on Nuclear Power Engineering in Space, May 1990.

[8]Morozov, A. I., Shubin, A. P., and Elizarov, L. I., "Modern State and Future of Electric Propulsion Thrusters," Anniversary Specialist Conf. on Nuclear Power Engineering in Space, May 1990.

[9]Haas, J. M., Gulczinski, F. S., Gallimore, A. D., Spanjers, G. G., and Spores, R. A., "Performance Characteristics of a 5-kW Laboratory Hall Thruster," AIAA Paper 98-3503, July 1998.

[10]Randolph, T., Pencil, E., and Manzella, D., "Far-Field Plume Contamination and Sputtering of the Stationary Plasma Thruster," AIAA Paper 94-2855, June 1994.

[11]Roussel, J. F., Bernard, J., and Garnier, Y., "Numerical Simulation of Induced Environment, Sputtering, and Contamination of Satellite due to Electric Propulsion," *Proceedings of the 2nd European Spacecraft Propulsion Conference*, 1997 pp. 517–522; also ESA Rept. SP-398, Aug. 1997.

[12]Manzella, D. H., "Stationary Plasma Thruster Plume Emissions," International Electric Propulsion Conf., Rept. IEPC-93-097, Sept. 1993.

[13]Vahrenkamp, R. P., "Measurement of Double Charged Ions in the beam of a 30-cm Mercury Bombardment Thruster," AIAA Paper 73-1057, Oct. 1973.

[14]Hutchinson, I., *Principles of Plasma Diagnostics*, 1st ed., Cambridge Univ. Press, New York, 1987, pp. 79–84.

[15]King, L. B., "Transport-Property and Mass Spectral Measurements in the Plasma Exhaust Plume of a Hall-Effect Space Propulsion System," Ph.D. Dissertation, Dept. of Aerospace Engineering, Univ. of Michigan, Ann Arbor, MI, May 1998.

[16]Sovey, J. S., "Improved Ion Containment Using a Ring-Cusp Ion Thruster," *Journal of Spacecraft and Rockets*, Vol. 21, No. 5, 1984, pp. 488–495.

[17]Patterson, M. J., "Performance Characteristics of Ring-Cusp Thrusters with Xenon Propellant," AIAA Paper 86-1392, June 1986.

[18]Kuang, Y.-Z., Guo-Qing, F.-L., and Yang, S.-T., "$E \times B$ Momentum Analyzer for Broad-Beam Ion Sources," AIAA Paper 87-1081, May 1987.

[19]Takegahara, H., Kasai, Y., "Beam Characteristics Evaluation of ETS-VI Xenon Ion Thruster," International Electric Propulsion Conf., Rept. IEPC-93-235, Sept. 1993.

[20]Pollard, J. E., "Plume Angular, Energy, and Mass Spectral Measurements with the T5 Ion Engine," AIAA Paper 95-2920, July 1995.

[21]Anderson, J. R., and Fitzgerald, D., "Fullerene Propellant Research for Electric Propulsion," AIAA Paper 96-3211, July 1996.

[22]Nakayama, Y., and Takegahara, H., "C_{60} Application to Ion Thruster—Inspection of Ionized and Extracted Particle," International Electric Propulsion Conf., Rept. IEPC-97-076, Aug. 1997.

[23]Kim, S. W., "Experimental Investigations of Plasma Parameters and Species-Dependent Ion Energy Distribution in the Plasma Exhaust Plume of a Hall Thruster," Ph.D. Dissertation, Dept. of Aerospace Engineering, Univ. of Michigan, Ann Arbor, MI, Aug. 1999.

[24]Myers, R., and Manzella, D., "Stationary Plasma Thruster Plume Characteristics," International Electric Propulsion Conf., Rept. IEPC Paper 93-096, Sept. 1993.

[25]Manzella, D., and Sankovic, J., "Hall Thruster Ion Beam Characterization," AIAA Paper 95-2927, July 1995.

[26]Gulczinski, F. S., III, "Examination of the Structure and Evolution of Ion Energy Properties of a 5-kW Class Laboratory Hall Effect Thruster at Various Operational Conditions," Ph.D. Dissertation, Dept. of Aerospace Engineering, Univ. of Michigan, Ann Arbor, MI, Aug. 1999.

[27]Raizer, Y. P., *Gas Discharge Physics*, 1st ed., Springer-Verlag, Berlin, 1991, pp. 96, 97.

[28]Rundle, H. W., Clark, D. R., and Deckers, J. M., "Electron Energy Distribution Functions in an O_2 Glow Discharge," *Canadian Journal of Physics*, Vol. 51, No. 2, 1973, pp. 144–148.

[29]Foster, J. E., "An Investigation of the Influence of a Transverse Magnetic Field on the Formation of Large Anode Fall Voltages in Low-Pressure Arcs," Ph.D. Dissertation, Dept. of Applied Physics, Univ. of Michigan, Ann Arbor, MI, Dec. 1996.

[30]Bishaev, A., and Kim, V., "Local Plasma Properties in a Hall-Current Accelerator with an Extended Acceleration Zone," *Soviet Physics, Technical Physics*, Vol. 23, No. 5, 1978, pp. 1055–1057.

[31]Randolph, T., Day, M., Kim, V., Kaufman, H., Zhurin, V., and Kozubsky, K., "Facility Effects on SPT Thruster Testing," International Electric Propulsion Conf., Rept. IEPC Paper 93-093, Sept. 1993.

[32]Lafferty, J. M., *Foundations of Vacuum Science and Technology*, 1st ed., Vol. 4, Wiley, New York, 1988, p. 404.

[33]Haas, J. M., and Gallimore, A. D., "Characterization of Interior Plasma Structure of a 5-kW-Class Hall Thruster," International Electric Propulsion Conf., Rept. IEPC Paper 99-078, Oct. 1999.

[34]King, L. B., and Gallimore, A. D., "A Gridded Retarding Pressure Sensor for Ion and Neutral Particle Analysis in Flowing Plasmas," *Review of Scientific Instruments*, Vol. 68, No. 2, 1997, pp. 1183–1188.

I. D. Boyd
Associate Editor